The Hyperluminous, Dust-obscured Quasar W2246–0526 at $z = 4.6$: Detection of Parsec-scale Radio Activity

Lulu Fan (范璐璐)[1,2,3] , Wen Chen (陈文)[4,5] , Tao An (安涛)[6] , Fu-Guo Xie (谢富国)[7] , Yunkun Han (韩云坤)[4] ,
Kirsten K. Knudsen[8] , and Jun Yang (杨军)[8]

[1] CAS Key Laboratory for Research in Galaxies and Cosmology, Department of Astronomy, University of Science and Technology of China, Hefei 230026, People's Republic of China; llfan@ustc.edu.cn
[2] School of Astronomy and Space Sciences, University of Science and Technology of China, Hefei, Anhui 230026, People's Republic of China
[3] Shandong Provincial Key Lab of Optical Astronomy and Solar-Terrestrial Environment, Institute of Space Science, Shandong University, Weihai, 264209, People's Republic of China
[4] Yunnan Observatories, Chinese Academy of Sciences, 396 Yangfangwang, Guandu District, Kunming, 650216, People's Republic of China
[5] University of Chinese Academy of Sciences, No.19(A) Yuquan Road, Shijingshan District, Beijing, 100049, People's Republic of China
[6] Key Laboratory of Radio Astronomy, Shanghai Astronomical Observatory, 80 Nandan Road, 200030, Shanghai, People's Republic of China
[7] Key Laboratory for Research in Galaxies and Cosmology, Shanghai Astronomical Observatory, Chinese Academy of Sciences, 80 Nandan Road, Shanghai 200030, People's Republic of China
[8] Department of Space, Earth and Environment, Chalmers University of Technology, Onsala Space Observatory, SE-439 92 Onsala, Sweden; jun.yang@chalmers.se
Received 2020 September 22; revised 2020 November 17; accepted 2020 November 28; published 2020 December 23

Abstract

WISE J224607.56−052634.9 (W2246−0526) is a hyperluminous ($L_{bol} \approx 1.7 \times 10^{14} L_\odot$), dust-obscured, and radio-quiet quasar at redshift $z = 4.6$. It plays a key role in probing the transition stage between dusty starbursts and unobscured quasars in the coevolution of galaxies and supermassive black holes (SMBHs). To search for the evidence of the jet activity launched by the SMBH in W2246−0526, we performed very long baseline interferometry observations of its radio counterpart with the European VLBI Network (EVN) plus the enhanced Multi Element Remotely Linked Interferometer Network (e-MERLIN) at 1.66 GHz and the Very Long Baseline Array (VLBA) at 1.44 and 1.66 GHz. The deep EVN plus e-MERLIN observations detect a compact (size $\leqslant 32$ pc) sub-mJy component contributing about 10% of its total flux density, which spatially coincides with the peak of dust continuum and [C II] emissions. Together with its relatively high brightness temperature ($\geqslant 8 \times 10^6$ K), we interpret the component as a consequence of nonthermal radio activity powered by the central SMBH, which likely originates from a stationary jet base. The resolved-out radio emission possibly come from a diffuse jet, quasar-driven winds, or both, while the contribution by star formation activity is negligible. Moreover, we propose an updated geometry structure of its multiwavelength active nucleus and shed light on the radio quasar selection bias toward the blazars at $z > 4$.

Unified Astronomy Thesaurus concepts: High-redshift galaxies (734); Quasars (1319); Radio continuum emission (1340); High-luminosity active galactic nuclei (2034)

1. Introduction

Under the framework of galaxy evolution through major mergers (e.g., Hopkins et al. 2008; Somerville & Davé 2015), dust-obscured quasars, hosting both intense star formation and active galactic nucleus (AGN) activities, represent the key transition stage between dusty starbursts and unobscured quasars. Therefore, they are excellent candidates for studying the coevolution of the massive galaxies and their central supermassive black holes (SMBHs). By using NASA's Wide-field Infrared Survey Explorer mission (Wright et al. 2010), a new population of hyperluminous, dust-obscured galaxies (so-called Hot DOGs) have been discovered (Eisenhardt et al. 2012; Wu et al. 2012), which have then been revealed as the extremely luminous ($L_{bol} \approx 10^{13.0-14.5} L_\odot$), merger-driven, heavily obscured quasars at high redshifts ($z \sim 1-4.6$) by the follow-up multiwavelength studies (e.g., Piconcelli et al. 2015; Tsai et al. 2015; Assef et al. 2016; Fan et al. 2016a, 2016b, 2017, 2018b; Ricci et al. 2017; Zappacosta et al. 2018).

W2246−0526, a Hot DOG at $z \sim 4.6$, is extremely luminous and massive, with a bolometric luminosity $L_{bol} \approx 1.7 \times 10^{14} L_\odot$ and a stellar mass $M_\star = 4.3 \times 10^{11} M_\odot$ (Fan et al. 2018a). It hosts a central SMBH with a black hole mass $M_{BH} \sim 4 \times 10^9 M_\odot$, accreting at a super-Eddington ratio, $\lambda_{Edd} = 2.8$ (Tsai et al. 2018). According to the Hubble Space Telescope (HST) near-IR image

W2246−0526 is likely merging with its close companion galaxy (Fan et al. 2016a). With Atacama Large Millimeter/submillimeter Array (ALMA) [C II] spectra and dust continuum imaging, W2246−0526 is confirmed to be accreting from at least three companion galaxies (Díaz-Santos et al. 2018). Spatially resolved ALMA [C II] observations have shown that it is unstable in terms of the energy and momentum that are being injected into the interstellar medium (ISM), strongly suggesting that the gas is being blown away isotropically (Díaz-Santos et al. 2016). All these results are consistent with the merger-driven evolutionary scenario, suggesting that W2246−0526 is in a key transitionary stage of massive galaxy evolution and on the road to becoming an unobscured quasar.

Free of obscuration, a radio wave has the advantage that it can penetrate deep into the centers of these dusty host galaxies. Recently, Patil et al. (2020) presented the subarcsecond-resolution imaging of a mid-infrared and radio-selected sample with 155 heavily obscured, ultraluminous quasars (Lonsdale et al. 2015), which revealed the compact radio structure in the majority of the sources in their sample. Utilizing the European VLBI Network (EVN), Frey et al. (2016) performed very long baseline interferometry (VLBI) observations of the radio counterparts of four Hot DOGs at $z \sim 2$. All four Hot DOGs were successfully detected at 1.7 GHz in the EVN images.
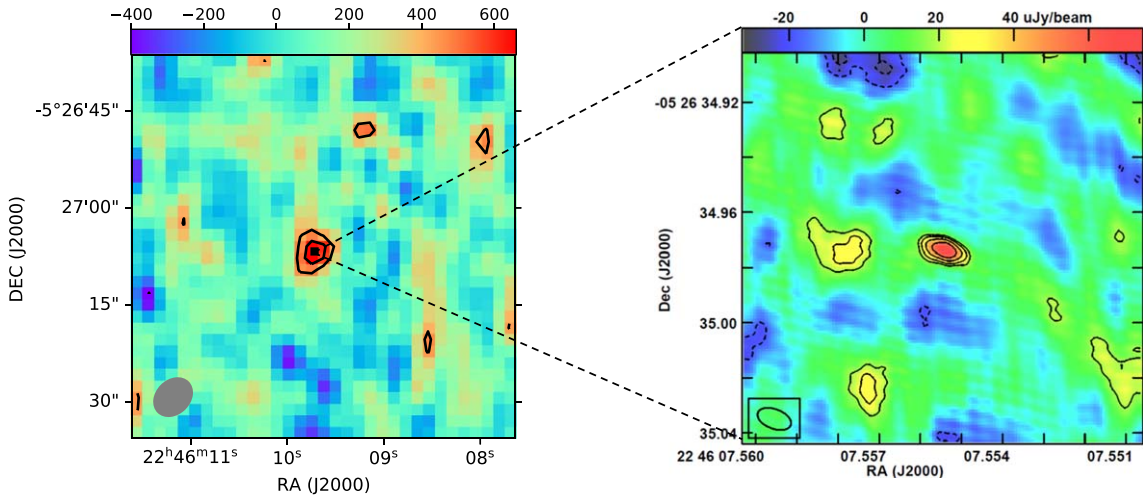
Figure 1. Radio observations of W2246−0526. Left: the $1' \times 1'$ FIRST cutout image of W2246−0526. The contours are at the 2.5σ and 3.5σ levels. The beam size is shown in the bottom left corner. Right: the EVN plus e-MERLIN image of the compact component in W2246−0526 at 1.66 GHz. The image size is $2'' \times 2''$. The contours start at 18.4 μJy beam^{-1} (2.5σ) and increase by factors of $-1.4, -1, 1, 1.4, 2,$ and 2.8. Only the central peak feature has a brightness (66 μJy beam^{-1}) of $> 5\sigma$ and thus can be firmly identified as an astrophysical source. The naturally weighted synthesized beam has dimensions of 12.7 mas $\times$ 6.3 mas (82.6 pc $\times$ 41.0 pc) at a position angle of $72°$ and is plotted in the bottom left corner.

The VLBI imaging results support that radio jets have already started in the transition phase where starburst and AGN activities coexist. The previous work made by Frey et al. (2016) suggests that Hot DOGs with radio jets represent the earliest stage of the radio AGN evolution (e.g., An & Baan 2012; Patil et al. 2020).

W2246−0526 has a faint radio counterpart with a flux density of 0.62 ± 0.15 mJy at 1.33 GHz (see the left panel of Figure 1) in the Very Large Array (VLA) Faint Images of the Radio Sky (FIRST) Survey (Becker et al. 1995). We estimate that star formation activity can only contribute a small fraction of the total radio flux density, while AGN-related activity should dominate the radio emission. Here we report our new results of the high-resolution EVN plus e-MERLIN and the Very Long Baseline Array (VLBA) observations of W2246−0526. Throughout this work we assume a standard, flat Λ cold dark matter (ΛCDM) cosmology (see Komatsu et al. 2011), with $H_0 = 70$ km s^{-1} Mpc^{-1}, $\Omega_M = 0.3$, and $\Omega_\Lambda = 0.7$. The spatial scale at the distance of W2246−0526 is ~ 6.5 pc per milliarcsecond (mas).

2. Observations and Data Reduction

We observed W2246−0526 at the L band with the EVN plus e-MERLIN on 2019 May 25 and the VLBA on 2019 August 19. The observation configurations are summarized in Table 1.

The EVN plus e-MERLIN observations (project code: EY034) were performed at a central frequency of 1.66 GHz. The data recording rates were 1024 Mbps (16 subbands, dual polarization, 16 MHz per subband, 2-bit quantization) at the EVN stations and 512 Mbps (2 subbands, dual polarization, 64 MHz per subband, 2-bit quantization) at the e-MERLIN stations (CM, DA, KN, PI, DE). The data correlation was done by the EVN software correlator (SFXC; Keimpema et al. 2015) at the Joint Institute for VLBI, ERIC (JIVE) using standard correlation parameters of continuum experiments.

The VLBA observations (project code: BF130) were carried out at both 1.44 and 1.66 GHz simultaneously with its broadband L-band receivers. The observations had a total recording rate of 2048 Mbps: 4 subbands, 128 MHz per subband, dual polarization, 2-bit quantization, 1024 Mbps at 1.44 GHz, and 1024 Mbps at

Table 1
Summary of the VLBI Observations

Date (yymmdd)	ν_{obs} (GHz)	Time (hr)	Participating Radio Telescopes
190525	1.66	7.0	JB, EF, WB, MC, O8, UR, TR, HH, SV, ZC, IR, SR, CM, DA, KN, PI, DE
190819	1.44, 1.66	8.0	BR, FD, HN, KP, LA, MK, NL, OV, PT, SC

Note. The two-letter antenna codes are explained in Appendix A.

1.66 GHz. The data were correlated by the distributed FX software correlator (DiFX; Deller et al. 2007) at the National Radio Astronomy Observatory (NRAO) using the normal correlation parameters of continuum experiments (1 s integration time and 0.5 MHz frequency resolution).

All these observations were carried out in the phase-referencing mode. The compact radio source J2248−0541 (Beasley et al. 2002) had a correlation amplitude of ~ 0.13 Jy at 2.3 GHz on the long baselines of the VLBA on 2017 May 31 (Charlot et al. 2020), and was used as the phase referencing calibrator. In both EVN plus e-MERLIN and VLBA experiments, we used a nodding cycle time of ~ 4 minutes. The coordinate of J2248−0541 is R.A. (J2000) $= 22^h48^m00\overset{s}{.}0806$ and decl. (J2000) $= -05°41'18''\!.219$ in the source catalog of GSFC 2015a obtained from the Goddard Space Flight Center VLBI group.[9] Compared to its optical position (with an uncertainty of 0.5 mas) provided by the second data release of Gaia (Brown et al. 2018), the VLBI position has an offset: -0.9 mas in R.A. and -1.6 mas in decl. The angular distance between the target and calibrator is about $0°\!.53$.

The visibility data were calibrated using the NRAO Astronomical Image Processing System (AIPS version 31DEC19; Greisen 2003) software package. A PRIORI amplitude calibration was performed with the system temperatures and the antenna gain curves provided by each telescope. In the case of missing these calibration data, the nominal system equivalent flux densities

---

9 http://astrogeo.org/vlbi/solutions/rfc_2015a/

recorded in the EVN status table[10] were used. The ionospheric dispersive delays were corrected according to the maps of total electron content obtained from the Global Positioning System satellite observations. Phase errors due to the antenna parallactic angle variations were calibrated. After instrumental phase and delay correction were carried out via fringe-fitting on a short scan of the fringe finder 3C 454.3, the global fringe-fitting and bandpass calibration were performed. In the case of the VLBA data, we reduced the two 128 MHz subbands per polarization separately because of their large separation in frequency (∼220 MHz). To get the self-calibration solutions at the high-frequency solution, we split each 128 MHz subband into eight 16 MHz subbands at each frequency.

The calibrator J2248−0541 was imaged using iterations of the CLEAN and self-calibration (Stokes I) in the software package DIFMAP (version 2.5e; Shepherd et al. 1994), fringe-fitting and self-calibration (Stokes RR and LL) with the input of the new CLEAN image in AIPS. In each iteration, both the phase and amplitude self-calibration solutions were also applied to the target source, and the phase errors due to the calibrator structure were removed. The calibrator had a one-sided core–jet structure with total flux densities of 0.40 ± 0.02 Jy at 1.44 GHz and 0.33 ± 0.02 Jy at 1.66 GHz. We used the jet base, the most compact and brightest component, as the reference point in the phase-referencing calibration. After three iterations, the deconvolved Stokes I map using natural weighting reached an image noise level of $\sim 90\,\mu$Jy beam^{-1} in these VLBI images. Thanks to the quite small angular separation ($0\overset{\circ}{.}53$) between the calibrator and the target, the phase-referencing calibration worked at a reasonably accurate level. In the residual map of the target source using natural weighting, there are no $>5\sigma$ systematic errors (noise peaks, stripes, and rings). We plot the EVN and VLBA images of the phase-referencing calibrator J2248−0541 in Appendix B.

3. VLBI Imaging Results

The image of the EVN plus e-MERLIN observations of W2246−0526 is shown in the right panel of Figure 1. We detect a single unresolved source co-located with the position of W2246−0526 without self-calibration. The component has a peak brightness of $66\,\mu$Jy beam^{-1}. Compared to the image noise level $7.4\,\mu$Jy beam^{-1} in the residual map, the detection has a signal-to-noise ratio (S/N) of 8.9. We also fit the visibility data in the (u, v) plane with a circular Gaussian model in DIFMAP and measured the formal uncertainties via setting the reduced $\chi^2 = 1$. The component has a total flux density of $75 \pm 9\,\mu$Jy and an angular size (FWHM) of 0.3 ± 4.9 mas, indicating an unresolved source structure of $\leqslant 4.9$ mas. Using the radio core of the phase-referencing calibrator as the reference point, we carried out differential astrometry and then derived a position for W2246−0526, R.A. $= 22^{\rm h}46^{\rm m}07\overset{\rm s}{.}55542$ ($\sigma_{\rm ra} = 0.8$ mas) and decl. $= -05\degree26'34\overset{''}{.}9739$ ($\sigma_{\rm dec} = 0.6$ mas). Because the detection has a relatively low S/N, these formal uncertainties dominate the associated error budgets. The empirical 1σ systematic errors are small, 5% for the total flux density and ~ 0.3 mas for the position due to the residual phase errors of the phase-referencing calibration. We also searched for the more extended emission via trying a significant Gaussian taper of the visibility data with a value of 0.5 at 2 mega-wavelength or

excluding the long-baseline data; however, we did not detect any diffuse component in a field of 2×2 arcsec^2.

The core brightness temperature can be estimated as (e.g., Condon et al. 1982)

$$T_{\rm b} = 1.22 \times 10^9 \frac{S_{\rm obs}}{\nu_{\rm obs}^2 \theta_{\rm size}^2}(1 + z), \qquad (1)$$

where $S_{\rm obs}$ is the observed total flux density in mJy, $\nu_{\rm obs}$ is the observing frequency in GHz, $\theta_{\rm size}$ is the FWHM of the circular Gaussian model in mas, and z is the redshift. Because the component is unresolved, we take its 1σ error as an upper limit of its angular size. Thus, the component has $T_{\rm b} \geqslant 8 \times 10^6$ K.

With the input of the accurate position from the 1.66 GHz EVN plus e-MERLIN detection, we could also gain a marginal detection of W2246−0526 in the VLBA observations, S/N = 3.2 at 1.44 GHz. This is expected since the VLBA observations have a relatively higher image noise, $17\,\mu$Jy beam^{-1} at 1.44 GHz. The total flux density is $66 \pm 18\,\mu$Jy at 1.44 GHz. At 1.66 GHz, we failed to achieve a $\geqslant 3\sigma$ detection of the component because of the limited image sensitivity $23\,\mu$Jy beam^{-1}. We plot the VLBA images of W2246−0526 at 1.44 and 1.66 GHz in Appendix C.

4. Discussion

4.1. The Origin of Radio Emission in W2246–0526

The EVN plus e-MERLIN observations of W2246−0526 at 1.66 GHz detect an unresolved faint component with a size of $\leqslant 32$ pc and a radio luminosity of $L_{\rm R} = \nu L_\nu (1 + z)^{-1-\alpha} = 4.7 \times 10^{40}$ erg s^{-1}, assuming the spectral index $\alpha = 0$. Its position coincides with the peaks of the ALMA 212 μm dust continuum, [C II] emission and the HST near-IR images (Díaz-Santos et al. 2016, 2018; Fan et al. 2016a). The observed high brightness temperature ($\geqslant 8 \times 10^6$ K) cannot result from thermal emission, which generally has a $T_{\rm b} < 10^6$ K.

The VLBI component cannot be explained as a young radio supernova in the nucleus because its radio luminosity is two orders of magnitude higher than the known maximum luminosity ($L_{\rm R} \sim 5 \times 10^{38}$ erg s^{-1}) of young radio supernovae (e.g., Weiler et al. 2002). Instead, it may be naturally interpreted as the radio activity powered by the central accreting SMBH: a stationary jet base, a young out-moving jet, or a parsec-scale radio-emitting outflow. However, due to the limited image resolution and the absence of a spectral index measurement, we cannot distinguish among these possibilities. If it has a flat radio spectrum, it would be interpreted as the partially self-absorbed jet base. On the other hand, if it has a steep spectrum, it might result from either the out-moving jet or the parsec-scale outflow. However, considering the high value of the intrinsic emission frequency in the rest frame ($\nu_{\rm int} = \nu_{\rm obs}(1 + z) = 9.3$ GHz), the flat-spectrum radio emission is more likely to have a compact structure and high brightness temperature at a high frequency.

In order to constrain the spectral index on scales of a few arcseconds, we check the VLA Sky Survey (VLASS; Lacy et al. 2020) cutout image[11] of W2246−0526, which provides a nondetection and a 3σ upper limit at 3 GHz, $S_{\rm 3\,GHz} < 0.4$ mJy. Combining with the FIRST flux density, we can constrain the spectral index on scales of a few arcseconds ($\alpha < -0.7$). Thus, we assume a steep radio spectrum with a spectral index $\alpha = -0.8$ to derive the flux density at 1.4 GHz from EVN

---

plus e-MERLIN flux density at 1.66 GHz, which is only 86 μJy, 14% of the FIRST flux density observed on 2011 March 19. The intrinsic time interval between FIRST and our observation is $8(1 + z)^{-1} \approx 1.5$ yr. Typically, the radio luminosity variation is weak among nonblazar sources on the short timescale. Thus, the flux difference is most likely due to some low-brightness diffuse radio emission that is completely resolved out in the EVN image. The extended radio emission can come from intense star formation or AGN activities (jet or outflow). The derived star formation rate (SFR) of W2246 -0526 is about 500 $M_\odot$ yr^{-1} based on the IR luminosity (Díaz-Santos et al. 2018; Fan et al. 2018a). The corresponding radio power can be estimated from the conversion relation (Murphy et al. 2011)

$$\left(\frac{P_{1.4\,\mathrm{GHz}}}{\mathrm{erg\,s^{-1}\,Hz^{-1}}}\right) = 1.6 \times 10^{28}\left(\frac{\mathrm{SFR}_{1.4\,\mathrm{GHz}}}{M_\odot\,\mathrm{yr}^{-1}}\right). \qquad (2)$$

The corresponding flux density $S_{1.4\,\mathrm{GHz}}$ can be calculated by the equation

$$S_{1.4\,\mathrm{GHz}} = \frac{P_{1.4\,\mathrm{GHz}}}{4\pi D_{\mathrm{L}}^2(1 + z)^{-1-\alpha}}, \qquad (3)$$

where D_{L} is the luminosity distance of W2246-0526. We get $S_{1.4\,\mathrm{GHz}} = 5.3\,\mu$Jy, which is only 1% of the extended radio emission. Therefore, the majority of the radio emission resolved out with EVN plus e-MERLIN could be associated with the AGN-related activity (jet and/or outflow).

The significantly overresolved VLBI radio structure in W2246-0526 is frequently seen among these IR to submillimeter luminous but radio-quiet (or weak) sources (e.g., Frey et al. 2016; Chen et al. 2020). Compared to the Hot DOGs at $z \sim 2$–3 observed by Frey et al. (2016), W2246-0526 represents the more energetic case locating at the higher redshift. The VLBI-detected component is more compact and likely includes a compact radio core. The best nearby ($z < 0.3$) analogy to W2246-0526 might be the optically luminous quasar PDS 456 at $z = 0.184$. PDS 456 has a $\sim 10^9\,M_\odot$ black hole accreting at the Eddington rate, both of which are similar to those of our target. The VLBI observations of PDS 456 revealed a quite complex radio nucleus consisting of some very extended emission and a faint jet, including a candidate radio core at 1.66 GHz (Yang et al. 2021). At the higher frequency >5 GHz, only the candidate radio core would be detectable because of its partially optically thick radio spectrum (Yang et al. 2019, 2021).

4.2. The Heavily Dust-obscured, Radio-quiet Quasar at High Redshift

According to the spectral energy distribution (SED) modeling on the rest-frame UV/optical-to-far-IR of W2246-0526 (Fan et al. 2018a), we estimated the unattenuated flux density at 4400 Å (B band) $f_{\mathrm{B}} = 29\,\mu$Jy. The radio flux density at 5 GHz f_{R} is estimated by extrapolating from $f_{1.4\,\mathrm{GHz}}$. The radio-loudness $R = f_{\mathrm{R}}/f_{\mathrm{B}}$ of W2246-0526 is 1.1 by taking the EVN value $f_{1.4\,\mathrm{GHz}} = 86\mu$Jy, or 7.7 by taking the FIRST value $f_{1.4\,\mathrm{GHz}} = 620\mu$Jy. In either case, the radio-loudness R is less than 10. Therefore, W2246-0526 will be classified as a radio-quiet quasar (Kellermann et al. 1989). The radio-loudness R has been found to be strongly inversely correlated with the

accretion ratio λ (Ho 2002; Sikora et al. 2007). Based on the $R - \lambda$ relation given by Ho (2002), the expected radio-loudness is 1.1 from the Eddington ratio of W2246-0526 $\lambda_{\mathrm{Edd}} = 2.8$ (Tsai et al. 2018), which is in good agreement with our above estimation.

W2246-0526 has been suggested to be blowing out its ISM isotropically, based on the finding of a large uniform velocity dispersion of the [C II] emission (Díaz-Santos et al. 2016). Shocks, which propagate through the host galaxy as a result of quasar-driven winds, can accelerate relativistic electrons in quasar-driven winds and produce the nonthermal synchrotron radio emission with $\nu L_\nu \sim 10^{-5} L_{\mathrm{AGN}}$ on scales > 0.1 kpc (Nims et al. 2015). Given the bolometric luminosity of W2246-0526 ($L_{\mathrm{bol}} \sim 1.7 \times 10^{14} L_\odot$), the expected radio emission will be about 10^{42-43} erg s^{-1}, which is generally consistent with the observed radio emission at 1.4 GHz. The origin of the radio emission from quasar-driven winds has been supported by the observed correlation between the radio luminosity and the velocity dispersion of [O III]-emitting ionized gas in low-redshift (Zakamska & Greene 2014) and high-redshift, radio-quiet quasars (Hwang et al. 2018). However, compact, steep-spectrum, low-power jets launched by central SMBHs can also produce the radio emission with a similar luminosity to the observed value of W2246-0526 (Leipski et al. 2006). In particular, a jet is expected to be formed in W2246-0526, which has high gas and dust contents on the scale of $2 \sim 3$ kpc (Fan et al. 2016b; Díaz-Santos et al. 2018), resulting in efficient confinement and formation of diffuse jets.

As discussed above, quasar-driven winds and/or a diffuse jet can dominate the extended radio emission in W2246-0526, while star formation can only contribute a small fraction of $\sim 1\%$. We propose a possible scenario of the inner region of W2246-0526, which is shown as a cartoon in Figure 2. The heavy obscuration is suggested by the result of infrared SED decomposition, where the covering factor of the clumpy dust torus is close to 1 (Fan et al. 2016b). The heavily obscured dust structure together with a relativistic jet is exactly what had been expected by Ghisellini & Sbarrato (2016), in order to explain the disagreement between the observed and misaligned quasar numbers at $z > 4$ (Volonteri et al. 2011). Radio sources like W2246-0526 show faint optical emission due to the obscuration, and thus cannot be selected by the match of radio and optical catalogs. Only the line of sight along the jet can observe the unattenuated optical emission from the accretion disk and the broad emission line regions (BLRs). The selection is then biased toward the blazars.

5. Summary

Based on the high-resolution radio observations of the hyperluminous, dust-obscured, quasar W2246-0526 at $z = 4.6$ with the EVN plus e-MERLIN and the VLBA, we achieved an S/N ~ 9 detection of an unresolved component ($\leqslant 32$ pc) at 1.66 GHz in the nucleus. The parsec-scale compact component has a brightness temperature $T_{\mathrm{b}} \geqslant 8 \times 10^6$ K, which can be naturally explained as the radio activity powered by the central accreting SMBH: a stationary jet base, an out-moving jet, or radio-emitting winds. The flux density of the compact-core component ($75 \pm 9\,\mu$Jy) only accounts for about 10% of the known FIRST flux density. Given the SFR$\sim$500 $M_\odot$ yr^{-1} of W2246-0526, the corresponding radio flux density from star formation is only 1% of the extended radio emission that is
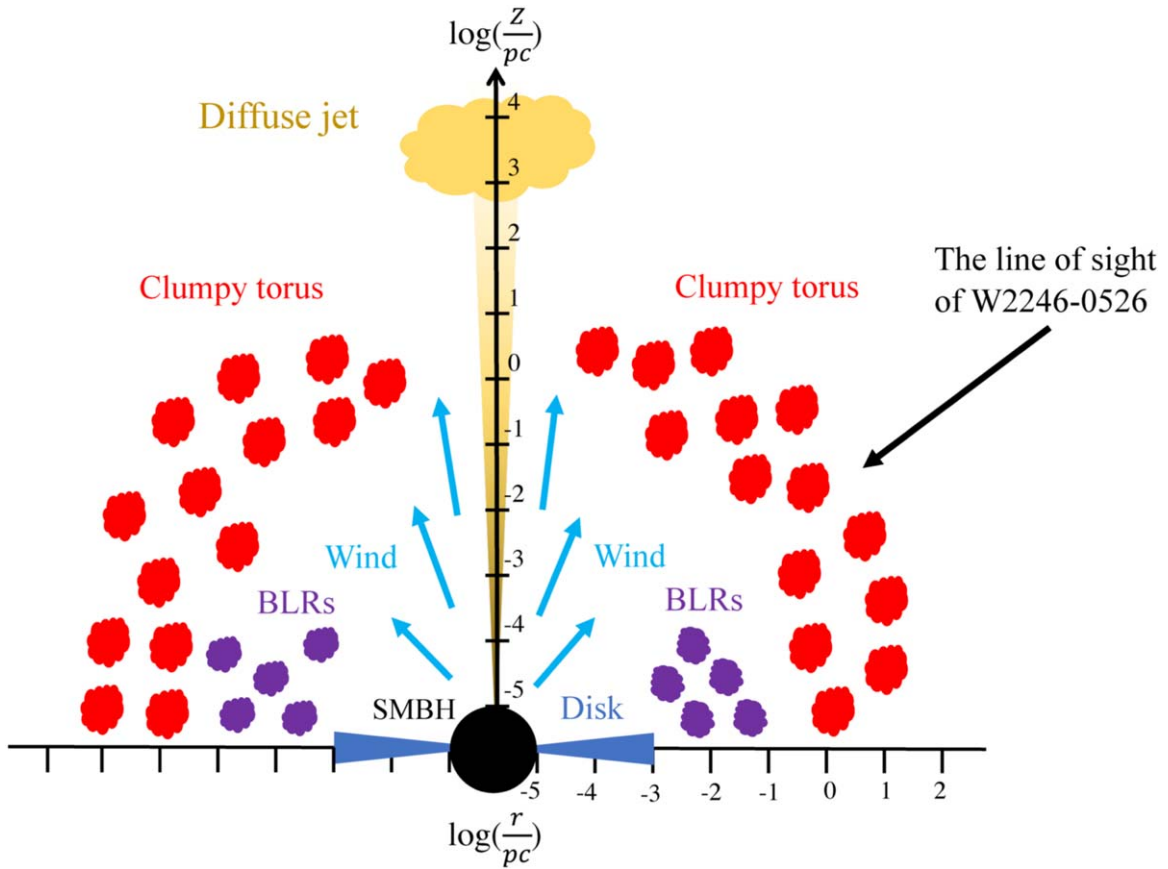
Figure 2. A cartoon of the proposed structure in the inner region of W2246−0526, based on the AGN physical model in Ramos Almeida & Ricci (2017). Radio emissions in W2246−0526 mainly come from a stationary jet base or a newly emerging moving-out jet (the unresolved compact-core component), and the quasar-driven radio-emitting winds and/or a diffuse jet (the extended radio emission). The line of sight of W2246−0526 and the possible jet are misaligned. W2246−0526 is optically faint due to the heavy dust obscuration (the covering factor of dust torus is close to 1), and thus can be missed by optical surveys, such as the Sloan Digital Sky Survey (SDSS).

completely resolved out with EVN plus e-MERLIN. Therefore, the majority of the VLBI-undetected radio emission could be associated with the quasar-driven winds and/or a diffuse jet. The nature of this diffuse radio emission can be tested in the future using current instruments like the VLA (A-config). Compared to the heavily obscured, hyperluminous quasars at $z \sim 0.4$–3 (Frey et al. 2016; Patil et al. 2020), W2246−0526 represents the most luminous case ($L_{\rm bol} = 1.7 \times 10^{14}\,{\rm erg\,s^{-1}}$) locating at the higher redshift, and the VLBI-detected component is more compact.

The radio-loudness R is estimated to be 1.1 or 7.7 depending on the choice of the radio flux density of the EVN plus e-MERLIN value or the FIRST value. Thus, W2246−0526 is a rare, radio-quiet quasar with high-resolution VLBI detection, while most if not all of those VLBI-detected quasars at $z > 4.5$ are radio-loud (Coppejans et al. 2016). Combining the possible evidence of jet activity and the heavy dust obscuration in W2246−0526, we propose a possible scenario of its inner region. The proposed scenario is consistent with the expectation by Ghisellini & Sbarrato (2016) in order to explain the disagreement of the observed number among blazars and misaligned radio quasars at $z > 4$.

Appendix A
## The Telescopes Participating in the VLBI Observations

A total of 17 telescopes participated in the deep EVN plus e-MERLIN observations: Jodrell Bank Mk2 (JB), Westerbork (WB, single dish), Effelsberg (EF), Medicina (MC), Onsala (O8), Urumqi (UR), Toruń (TR), Hartebeesthoek (HH), Svetloe (SV), Zelenchukskaya (ZC), Irbene (IR), Sardinia (SR), Cambridge (CM), Darnhall (DA), Knockin (KN), Pickmere (PI), and Defford (DE).

The participating telescopes in the VLBA observations were St. Croix (SC), Hancock (HN), North Liberty (NL), Fort Davis (FD), Los Alamos (LA), Pie Town (PT), Kitt Peak (KP), Owens Valley (OV), Brewster (BR), and Maunakea (MK).

Appendix B
EVN and VLBA Images of the Phase-referencing Calibrator

We provide the EVN and VLBA images of the phase-referencing calibrator J2248−0541 in Figure 3.
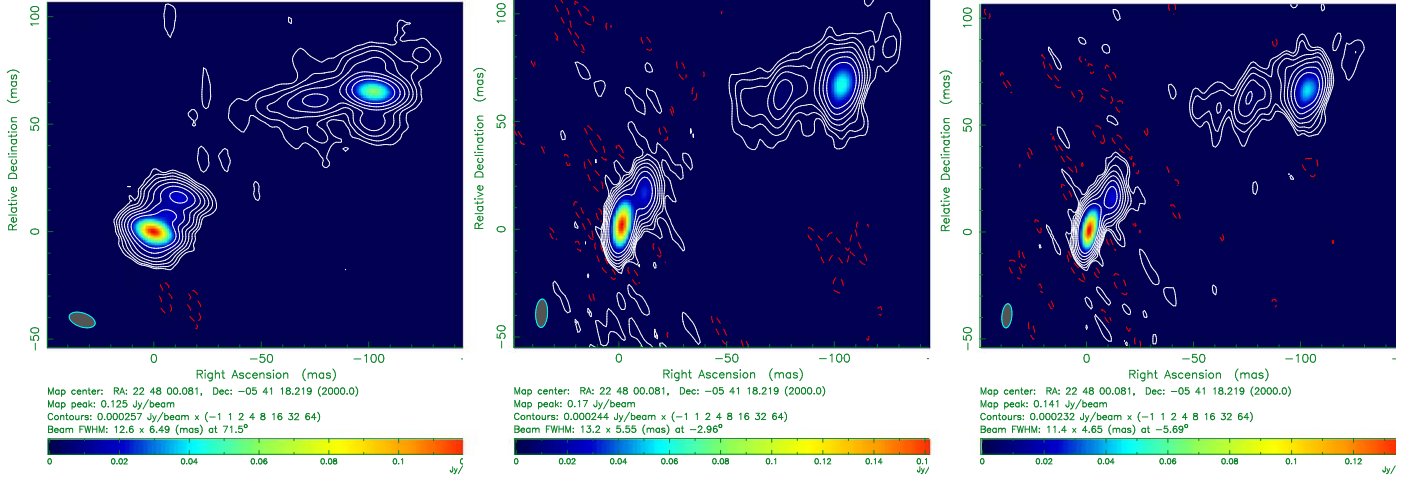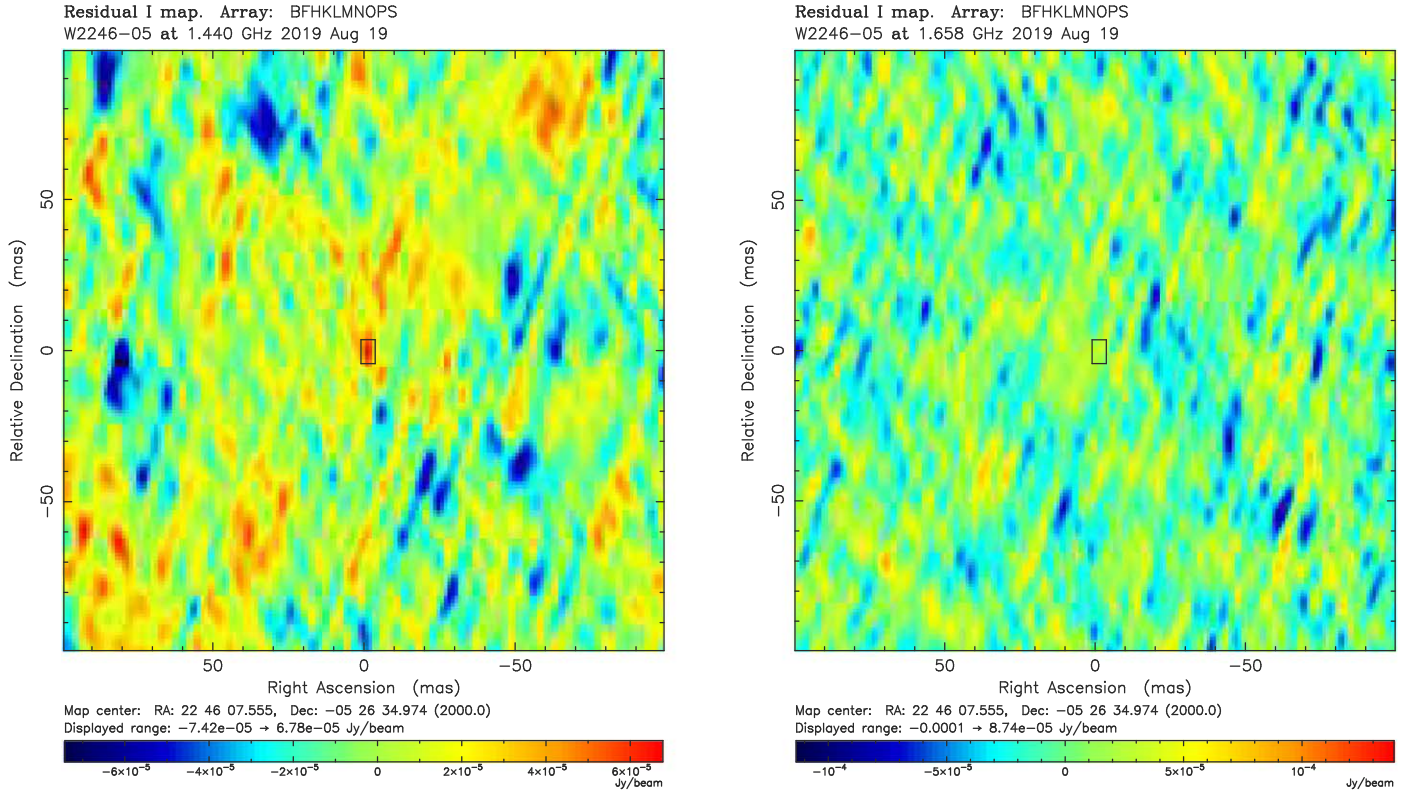

Figure 3. The VLBI images of the phase-referencing calibrator J2248−0541 at 1.44 GHz by EVN (left panel), 1.44 GHz by VLBA (middle panel), and 1.66 GHz by VLBA (right panel). The first contours are at the 3σ level.

Appendix C
VLBA Images of W2246−0526

We provide the VLBA images of W2246−0526 in Figure 4.

Figure 4. The dirty maps of W2246−0526 observed by the VLBA simultaneously at 1.44 GHz (left panel) and 1.66 GHz (right panel). The rectangles on both panels mark the position of the compact component in W2246−0526 detected by the EVN plus e-MERLIN. We gain a marginal detection (S/N = 3.2) at 1.44 GHz, while we fail to achieve a $\geqslant 3\sigma$ detection at 1.66 GHz.

ORCID iDs

Lulu Fan (范璐璐) ⊙ https://orcid.org/0000-0003-4200-4432
Wen Chen (陈文) ⊙ https://orcid.org/0000-0002-5519-0628
Tao An (安涛) ⊙ https://orcid.org/0000-0003-4341-0029
Fu-Guo Xie (谢富国) ⊙ https://orcid.org/0000-0001-9969-2091
Yunkun Han (韩云坤) ⊙ https://orcid.org/0000-0002-2547-0434
Kirsten K. Knudsen ⊙ https://orcid.org/0000-0002-7821-8873
Jun Yang (杨军) ⊙ https://orcid.org/0000-0002-2322-5232

References

An, T., & Baan, W. A. 2012, ApJ, 760, 77
Assef, R. J., Walton, D. J., Brightman, M., et al. 2016, ApJ, 819, 111
Beasley, A. J., Gordon, D., Peck, A. B., et al. 2002, ApJS, 141, 13
Becker, R. H., White, R. L., & Helfand, D. J. 1995, ApJ, 450, 559
Brown, A. G. A. & et al., Gaia Collaboration 2018, A&A, 616, A1
Charlot, P., Jacobs, C. S., Gordon, D., et al. 2020, A&A, 644, A159
Chen, H., Garrett, M. A., Chi, S., et al. 2020, A&A, 638, A113
Condon, J. J., Condon, M. A., Gisler, G., & Puschell, J. J. 1982, ApJ, 252, 102
Coppejans, R., Frey, S., Cseh, D., et al. 2016, MNRAS, 463, 3260
Deller, A. T., Tingay, S. J., Bailes, M., & West, C. 2007, PASP, 119, 318
Díaz-Santos, T., Assef, R. J., Blain, A. W., et al. 2016, ApJL, 816, L6
Díaz-Santos, T., Assef, R. J., Blain, A. W., et al. 2018, Sci, 362, 1034
Eisenhardt, P. R. M., Wu, J., Tsai, C.-W., et al. 2012, ApJ, 755, 173
Fan, L., Gao, Y., Knudsen, K. K., et al. 2018a, ApJ, 854, 157
Fan, L., Han, Y., Fang, G., et al. 2016a, ApJL, 822, L32
Fan, L., Han, Y., Nikutta, R., Drouart, G., & Knudsen, K. K. 2016b, ApJ, 823, 107
Fan, L., Jones, S. F., Han, Y., & Knudsen, K. K. 2017, PASP, 129, 124101
Fan, L., Knudsen, K. K., Fogasy, J., et al. 2018b, ApJL, 856, L5
Frey, S., Paragi, Z., Gabányi, K. É., et al. 2016, MNRAS, 455, 2058

Ghisellini, G., & Sbarrato, T. 2016, MNRAS, 461, L21
Greisen, E. W. 2003, in Information Handling in Astronomy: Historical Vistas, Vol. 285, ed. A. Heck (Dordrecht: Kluwer), 109
Ho, L. C. 2002, ApJ, 564, 120
Hopkins, P. F., Hernquist, L., Cox, T. J., et al. 2008, ApJS, 175, 356
Hwang, H.-C., Zakamska, N. L., Alexandroff, R. M., et al. 2018, MNRAS, 477, 830
Keimpema, A., Kettenis, M. M., Pogrebenko, S. V., et al. 2015, ExA, 39, 259
Kellermann, K. I., Sramek, R., Schmidt, M., et al. 1989, AJ, 98, 1195
Komatsu, E., Smith, K. M., Dunkley, J., et al. 2011, ApJS, 192, 18
Lacy, M., Baum, S. A., Chandler, C. J., et al. 2020, PASP, 132, 035001
Leipski, C., Falcke, H., Bennert, N., et al. 2006, A&A, 455, 161
Lonsdale, C. J., Lacy, M., Kimball, A. E., et al. 2015, ApJ, 813, 45
Murphy, E. J., Condon, J. J., Schinnerer, E., et al. 2011, ApJ, 737, 67
Nims, J., Quataert, E., & Faucher-Giguère, C.-A. 2015, MNRAS, 447, 3612
Patil, P., Nyland, K., Whittle, M., et al. 2020, ApJ, 896, 18
Piconcelli, E., Vignali, C., Bianchi, S., et al. 2015, A&A, 574, L9
Ramos Almeida, C., & Ricci, C. 2017, NatAs, 1, 679
Ricci, C., Assef, R. J., Stern, D., et al. 2017, ApJ, 835, 105
Shepherd, M. C., Pearson, T. J., & Taylor, G. B. 1994, BAAS, 26, 987
Sikora, M., Stawarz, Ł., & Lasota, J.-P. 2007, ApJ, 658, 815
Somerville, R. S., & Davé, R. 2015, ARA&A, 53, 51
Tsai, C.-W., Eisenhardt, P. R. M., Jun, H. D., et al. 2018, ApJ, 868, 15
Tsai, C.-W., Eisenhardt, P. R. M., Wu, J., et al. 2015, ApJ, 805, 90
Volonteri, M., Haardt, F., Ghisellini, G., et al. 2011, MNRAS, 416, 216
Weiler, K. W., Panagia, N., Montes, M. J., et al. 2002, ARA&A, 40, 387
Wright, E. L., Eisenhardt, P. R. M., Mainzer, A. K., et al. 2010, AJ, 140, 1868
Wu, J., Tsai, C.-W., Sayers, J., et al. 2012, ApJ, 756, 96
Yang, J., An, T., Zheng, F., et al. 2019, MNRAS, 482, 1701
Yang, J., Paragi, Z., Nardini, E., et al. 2021, MNRAS, 500, 2620
Zakamska, N. L., & Greene, J. E. 2014, MNRAS, 442, 784
Zappacosta, L., Piconcelli, E., Duras, F., et al. 2018, A&A, 618, A28